

Martensitic transition, ferromagnetic transition, and their interplay in the shape memory alloys $\text{Ni}_2\text{Mn}_{1-x}\text{Cu}_x\text{Ga}$

M. Kataoka

Department of Basic Sciences, Faculty of Science and Engineering, Ishinomaki Senshu University, Ishinomaki 986-8580, Japan

K. Endo, N. Kudo, and T. Kanomata

Faculty of Engineering, Tohoku Gakuin University, Tagajo 985-8537, Japan

H. Nishihara

Faculty of Science and Technology, Ryukoku University, Otsu 520-2194, Japan

T. Shishido and R. Y. Umetsu

Institute for Materials Research, Tohoku University, Sendai 980-8577, Japan

M. Nagasako and R. Kainuma

Department of Materials Science, Tohoku University, Sendai 980-8579, Japan

(Received 21 May 2010; revised manuscript received 20 October 2010; published 28 December 2010)

Magnetization and initial permeability measurements were done on the ferromagnetic shape memory alloys $\text{Ni}_2\text{Mn}_{1-x}\text{Cu}_x\text{Ga}$ ($0 \leq x \leq 0.4$). On the basis of the results, the phase diagram in the temperature-concentration plane was determined for this alloy system. The determined phase diagram is spanned by the paramagnetic austenite phase (I), paramagnetic martensite phase (II), ferromagnetic austenite phase (III), ferromagnetic martensite phase (IV), and the premartensite phase (V). It was found that the magnetostructural transitions between the phases I and IV can occur in the concentration region $0.23 \leq x \leq 0.30$ and that $\text{Ni}_2\text{Mn}_{1-x}\text{Cu}_x\text{Ga}$ has the characteristics of the phase diagram closely similar to those of the phase diagram of $\text{Ni}_{2+x}\text{Mn}_{1-x}\text{Ga}$. In order to understand the phase diagram, the phenomenological free energy as a function of the martensitic distortion and the magnetization was constructed and analyzed, where couplings between these order parameters in existing theories were improved. Satisfactory agreements between the theory and experiments were obtained except for the appearance of the premartensite phase. The analyses show that the biquadratic coupling term, together with a higher order coupling term, of the martensitic distortion to the magnetization, plays an important role in the interplay between the martensite phase and the ferromagnetic phase.

DOI: [10.1103/PhysRevB.82.214423](https://doi.org/10.1103/PhysRevB.82.214423)

PACS number(s): 75.50.-y, 64.60.Ej, 81.30.Kf

I. INTRODUCTION

Some Heusler-type alloys exhibit both the martensitic transition causing the shape memory effect and the ferromagnetic transition. The two phase transitions strongly affect each other, resulting in various fascinating phenomena. Some of such the phenomena are now considered to make these alloys useful as functional materials. In fact, the magnetic-field-induced strain (MFIS) and the magnetocaloric effect (MCE) observed in magnetic shape memory alloys have attracted considerable attention of researchers.

A MFIS was first found in Ni_2MnGa alloys in 1996.¹ This MFIS is brought about by the magnetic-field-induced rearrangement of martensite variants and has huge amounts over 9% while the work output stress is less than 5 MPa because of the limited driving force of the rearrangement. After this discovery, the MFIS, which is brought about by the magnetic-field-induced martensitic transition, has been reported on many magnetic shape memory alloys, such as Ni_2MnGa ,² Ni-Mn-In,³⁻⁸ Ni-Mn-Sn,⁹⁻¹² Fe-Mn-Ga (Ref. 13) alloys, etc. Especially, the MFIS of about 3% due to magnetic-field-induced reverse martensitic transition reported on $\text{Ni}_{45}\text{Co}_5\text{Mn}_{36.7}\text{In}_{13.3}$ and $\text{Ni}_{43}\text{Co}_7\text{Mn}_{39}\text{Sn}_{11}$ alloys attracted much attention on the group of these alloys.^{11,14} The

Ni-Mn-In- and Ni-Mn-Sn-based alloys, called metamagnetic shape memory alloys, show the MFIS at room temperature and yield high level of work output stress over 50 MPa.¹⁴⁻¹⁸ On the other hand, a large MCE due to the magnetic-field-induced martensitic transition in the Ni-Mn-based Heusler alloys was first reported on Ni-rich $\text{Ni}_{2+x}\text{Mn}_{1-x}\text{Ga}$. This phenomenon originates from the magnetostructural transition, i.e., a direct transition between a paramagnetic austenite phase to a ferromagnetic martensite phase,¹⁹⁻²⁵ which can be seen in the phase diagram of $\text{Ni}_{2+x}\text{Mn}_{1-x}\text{Ga}$ alloys.²⁶⁻³⁰ Very recently, a large MCE and a similar transition have been found also in $\text{Ni}_2\text{Mn}_{1-x}\text{Cu}_x\text{Ga}$ with $x=0.25$.³¹⁻³⁵ Nevertheless, there are only limited works on the martensitic and magnetic phase transitions in this alloy system.

Along with the experimental studies of these shape memory alloys, theoretical efforts have been done to understand the phase diagram which is spanned by the martensite phase, the ferromagnetic phase, and the phase with the coexisting martensitic and ferromagnetic states. In the phenomenological theories of $\text{Ni}_{2+x}\text{Mn}_{1-x}\text{Ga}$,^{27,29,36,37} the Landau free energy is expanded in powers of the bulk crystal strains e_{ij} as the order parameters of the martensitic phase transition and the magnetization components M_i as the order parameters of the ferromagnetic phase transition, i, j denoting the

crystal axes. Vasil'ev *et al.*^{27,37} proposed and studied the free energy which takes into account an anharmonic energy of the strain and the energy of a coupling between a linear term of the strain and a quadratic term of the magnetization, in addition to the usual free energies in the magnetostrain system. On the other hand, Khovaylo *et al.*²⁹ also considered the free energy including the anharmonic energies depending also on the volume strain, and showed that the cooperation of the magnetovolume strain and the anharmonic energy plays an important role in the phase diagram observed in $\text{Ni}_{2+x}\text{Mn}_{1-x}\text{Ga}$. Both the theories gave the scenarios for the appearance of a variety of phases in this compound. However, their scenarios of the appearance of the magnetostructural transition are different from each other and the question as to what mechanism dominates the phase diagram of the compound remains to be solved.

In this paper, the phase diagram of $\text{Ni}_2\text{Mn}_{1-x}\text{Cu}_x\text{Ga}$ is obtained experimentally by means of the permeability and differential-scanning-calorimetric measurements. The obtained phase diagram is analyzed by use of the reconstructed phenomenological free energy. The present analyses show that both the above scenarios by Vasil'ev *et al.* and by Khovaylo *et al.* are insufficient for understanding the observed phase diagram, but the presence of a biquadratic coupling, together with a higher order coupling, between the strain and the magnetization can explain successfully the phase diagram of the magnetic shape memory alloys.

In the following, Secs. II and III, experimental procedures and results on $\text{Ni}_2\text{Mn}_{1-x}\text{Cu}_x\text{Ga}$ are described to present its phase diagram. The subsequent Secs. IV–VI are devoted to give a phenomenological theory and its analyses to understand the phase diagram of $\text{Ni}_2\text{Mn}_{1-x}\text{Cu}_x\text{Ga}$. In Sec. VII, the phase diagram is calculated numerically by use of the developed theory and is compared with the observed one. Finally, concluding remarks are given in Sec. VIII.

II. EXPERIMENTAL PROCEDURE

The polycrystalline $\text{Ni}_2\text{Mn}_{1-x}\text{Cu}_x\text{Ga}$ ($0 \leq x \leq 0.40$) were prepared by repeated arc melting of the appropriate quantities of the constituent elements, namely, 99.99% pure Ni, 99.99% pure Mn, 99.99% pure Cu, and 99.9999% pure Ga, in an argon atmosphere. The reaction products with $x = 0.05, 0.10, 0.35, 0.40$ were pulverized, mixed, sealed in the evacuated silica tubes, heated at 850 °C for 3 days and then 600 °C for 1 day before being quenched into water. For the samples with $0.20 \leq x \leq 0.30$, the reaction products were heated at 900 °C for 3 days and then 600 °C for 1 day or 2 days. The phase characterization of the samples was carried out by x-ray powder diffraction measurements using $\text{Cu K}\alpha$ radiation.

The Curie temperature was determined by an ac transformer method. The primary and secondary coils were wound on the sample rod with about 1 mm in diameter. An ac current of a constant amplitude was let flow in the primary coil and the secondary voltage, which is directly proportional to initial permeability μ , was recorded as a function of temperature. The amplitude and the frequency of the ac magnetic field are about 7 Oe and 1 kHz, respectively. The magneti-

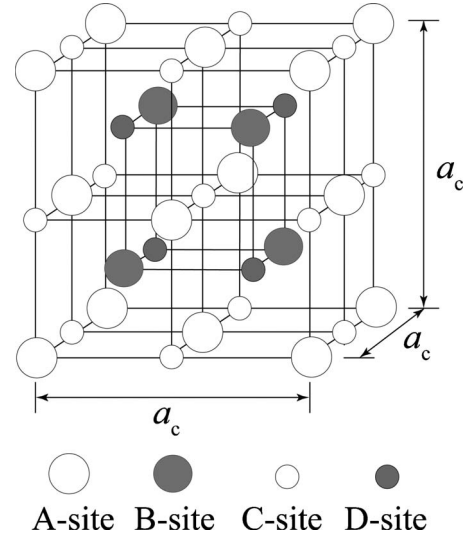


FIG. 1. Unit cell of the Heusler-type structure. The four different sites are denoted by A, B, C, and D.

zation M data were collected using a commercial superconducting quantum interference device magnetometer. Thermal analysis was carried out by differential scanning calorimetric (DSC) measurement, where the heating and cooling temperature rate was 10 K/min.

III. EXPERIMENTAL RESULTS

The Heusler $L2_1$ structure (space group: $Fm\bar{3}m$) is comprised of four interpenetrating fcc sublattices with A, B, C, and D sites. The A, B, C, and D sites are located at $(0,0,0)$, $(1/4, 1/4, 1/4)$, $(1/2, 1/2, 1/2)$, and $(3/4, 3/4, 3/4)$, respectively, as shown in Fig. 1. In Ni_2MnGa , Ni atoms occupy the A and C sites, and Mn atoms and Ga atoms the B and D sites, respectively. Figure 2(a) shows the observed x-ray powder diffraction pattern of the sample with $x=0.05$ at room temperature. All the experimental diffraction lines can be indexed with the cubic structure. The strong sharp (220)-peak confirms the presence of a single cubic phase. The intensities of the superlattice lines such as (111) and (200) agree well with the results calculated by assuming the $L2_1$ structure. These results ensure that the sample with $x=0.05$ has a fully ordered $L2_1$ structure. The lattice parameter a_c of the sample with $x=0.05$ is found to be 5.8095 Å. We observed a similar x-ray powder-diffraction pattern at room temperature for the sample with $x=0.20$, which indicates that the sample of $\text{Ni}_2\text{Mn}_{1-x}\text{Cu}_x\text{Ga}$ with $x=0.20$ crystallizes in the $L2_1$ structure at room temperature. Figure 2(b) shows the x-ray powder-diffraction pattern of the sample with $x=0.23$. Very recently, we established that the sample with $x=0.23$ crystallizes in a 14-layered monoclinic ($14M$) structure (space group: $C2/m$) well below the martensitic transition temperature. In Fig. 2(b), $(hkl)_c$ and $(hkl)_m$ indicate the Miller indices for the $L2_1$ and $14M$ structures, respectively. As shown in the figure, the cubic phase with the $L2_1$ structure and the monoclinic phase with the $14M$ structure coexist at room temperature in the sample with $x=0.23$. The lattice

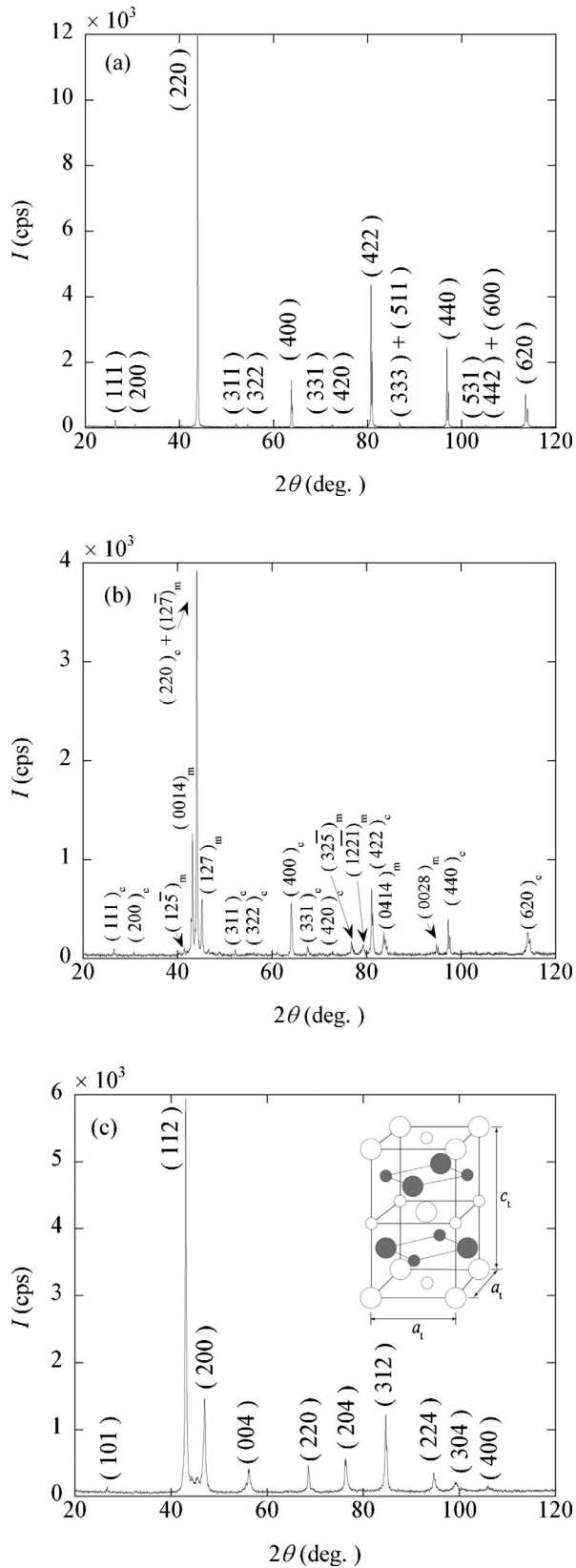


FIG. 2. X-ray powder-diffraction pattern at room temperature of (a) $\text{Ni}_2\text{Mn}_{0.95}\text{Cu}_{0.05}\text{Ga}$, (b) $\text{Ni}_2\text{Mn}_{0.77}\text{Cu}_{0.23}\text{Ga}$, and (c) $\text{Ni}_2\text{Mn}_{0.65}\text{Cu}_{0.35}\text{Ga}$. The inset in (c) shows the crystal structure of $\text{Ni}_2\text{Mn}_{0.65}\text{Cu}_{0.35}\text{Ga}$ in the martensite phase, where the symbols represent the four different sites A, B, C, and D as in Fig. 1.

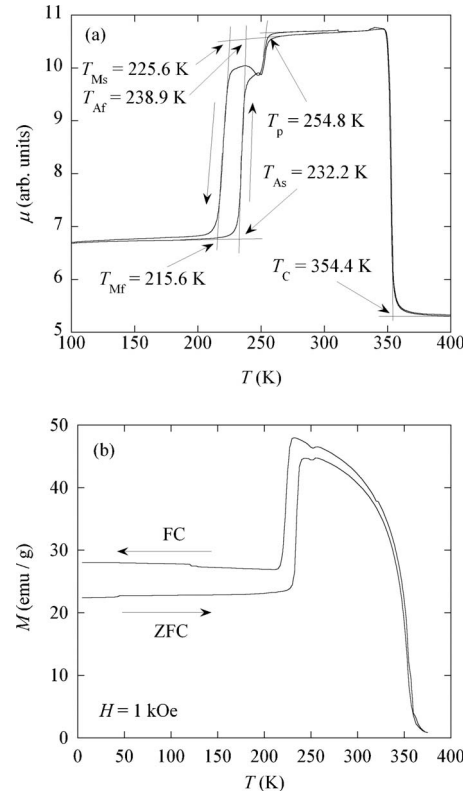


FIG. 3. Temperature dependences of (a) the initial permeability μ and (b) the magnetization M at 1 kOe for $\text{Ni}_2\text{Mn}_{0.95}\text{Cu}_{0.05}\text{Ga}$. The arrows along the curves in (a) show the cooling and heating processes. The arrows with ZFC and FC along the curves in (b) show the zero-field-cooling and field-cooling processes, respectively.

parameters of this sample were determined as $a_c = 5.7994 \text{ \AA}$ for the L_{21} phase and $a_m = 4.2146 \text{ \AA}$, $b_m = 5.5391 \text{ \AA}$, $c_m = 29.3166 \text{ \AA}$, and $\beta = 93.08^\circ$ for the $14M$ phase. Similarly, the x-ray powder-diffraction patterns of the samples with $x=0.25$ and 0.27 indicate that the cubic L_{21} phase and the $14M$ phase coexist at room temperature though the fraction of the $14M$ phase increases with increasing the concentration x . The x-ray powder diffraction pattern of the sample with $x=0.35$ at room temperature is shown in Fig. 2(c). All the diffraction lines can be indexed by assuming a DO_{22} -like crystal structure with the lattice parameters a_t and c_t as shown in the inset in Fig. 2(c). It is noted that this structure in the case of no lattice distortion and $c_t = \sqrt{2}a_t$ becomes the L_{21} structure itself, where an a_c axis is rotated by 45° from an a_t axis in a c_t plane and $a_c = c_t = \sqrt{2}a_t$. The intensities of all the diffraction lines agree well with the results calculated by assuming the crystal structure as shown in the inset in Fig. 2(c). The lattice parameters of this sample were determined as $a_t = 3.8862 \text{ \AA}$ and $c_t = 6.5360 \text{ \AA}$.

Figure 3(a) shows the temperature dependence of the initial permeability μ for the sample with $x=0.05$. The arrows along the curves in this figure show the heating and cooling processes. Abrupt changes in μ are observed around 230 K in the cooling and heating processes. These temperature variations of μ are similar to those of Ni_2MnGa .^{26–28} Therefore, the abrupt changes of μ are thought to correspond to a transition between the martensite phase and the austenite

phase. The martensitic-transition starting and finishing temperatures T_{Ms} and T_{Mf} , and the reverse martensitic-transition starting and finishing temperatures T_{As} and T_{Af} were defined as the cross points of the linear extrapolation lines of the μ versus T curves from both higher and lower temperature ranges as shown in the figure. The abrupt large decrease of μ with increasing temperature corresponds to the transition from the ferromagnetic state to the paramagnetic state. The Curie temperature T_C was also defined as the cross point of the linear extrapolation lines from higher and lower temperature ranges on the μ versus T curve. The Curie temperature is found to be 354.4 K for the sample with $x=0.05$. Moreover, an anomalous local dip is clearly observed above T_{Ms} and T_{As} . This dip starts and finishes around $T_p=254.8$ K on the μ versus T curves in both cooling and heating processes, which corresponds to a premartensitic transition temperature. It should be noted that the thermal hysteresis width at the premartensitic phase transition temperature is negligible. Wang *et al.* observed the thermal hysteresis of 10 K at T_p for the stoichiometric Ni_2MnGa ($x=0$).²⁸ Fig. 3(b) shows the temperature dependence of the magnetization M measured in a zero-field-cooling (ZFC) and a field-cooling (FC) processes at the applied field of 1 kOe for the sample with $x=0.05$. The abrupt change of μ in Fig. 3(a) and the abrupt change in M in Fig. 3(b), which are related to each other, are ascribed to the martensitic transition. In addition to the anomalous dip around T_p on the μ versus T curve of this sample, the observed magnetization also gives a dip around T_p , as shown in Fig. 3(b). However, the latter dip is tiny in spite of the distinct dip in the μ versus T curve. Similar behavior was observed in the μ versus T and M versus T curves in $Ni_{1.95}Cu_{0.05}MnGa$.³⁸ Recently, Ohba *et al.* carried out the precise crystal structure analysis of Ni_2MnGa by using high-energy synchrotron radiation. According to their result, Ni_2MnGa in the premartensite phase shows a tiny distortion from the cubic structure in the austenite phase, which results in its crystal structure with an orthorhombic lattice.³⁹ Figures 4(a) and 4(b) show the temperature dependences of μ and M at 1 kOe for the sample with $x=0.15$, respectively. Similar μ versus T and M versus T curves were observed also for the samples with $x=0.10$ and 0.20 . The temperatures T_{Ms} , T_{Mf} , T_{As} , and T_{Af} of the sample with $x=0.15$, which characterize the martensitic transition, were determined as shown in Fig. 4(a). It should be noted that the anomalous local dip as seen in Fig. 3(a) is not observed on the μ versus T curves for the sample with $x=0.15$. As shown in Figs. 3(a) and 4(a), the martensitic transition temperature increases with increasing the concentration x . Figures 5(a) and 5(b) show the temperature dependences of μ and M at 1 kOe for the sample with $x=0.23$, respectively. Similar μ versus T , and M versus T curves were observed also for the samples with $x=0.25$, 0.27 and 0.30 . As shown in Figs. 5(a) and 5(b), μ and M decrease abruptly around 300 K, indicating that the magnetic transition between the ferromagnetic phase and the paramagnetic phase is the first-order type. We did not observe any anomaly below T_C on the μ versus T , and M versus T curves, so that T_M is considered to coincide with T_C . The $T_C(=T_M)$ was estimated to be 301.2 K for the sample with $x=0.23$, where T_C was defined to be $T_C=T_M=(T_{Ms}+T_{Af})/2$. The temperature dependences of μ and M at 1 kOe for the sample with

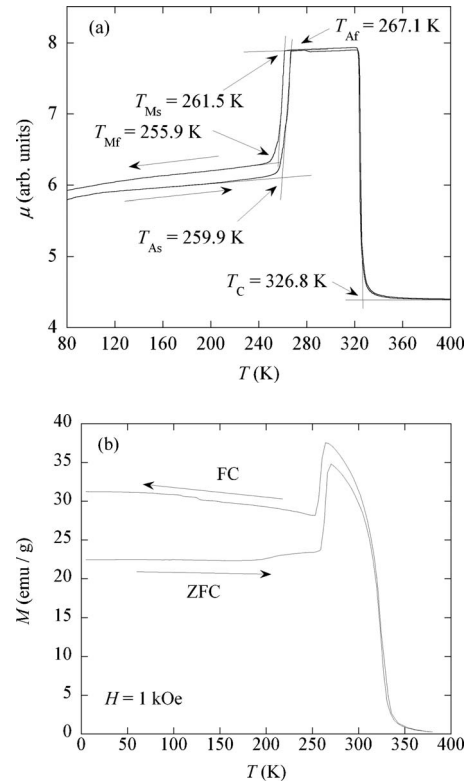


FIG. 4. Temperature dependences of (a) the initial permeability μ and (b) the magnetization M at 1 kOe for $Ni_2Mn_{0.85}Cu_{0.15}Ga$. The arrows along the curves in (a) show the cooling and heating processes. The arrows with ZFC and FC along the curves in (b) show the zero-field-cooling and field-cooling processes, respectively.

$x=0.35$ are shown in Figs. 6(a) and 6(b), respectively. The μ versus T , and M versus T curves in Figs. 6(a) and 6(b) are characteristic of ferromagnets with the ferromagnetic-paramagnetic second-order phase transition. As mentioned above, the x-ray powder-diffraction pattern at room temperature of the sample with $x=0.35$ shows the martensite phase with the DO_{22} -like crystal structure. To determine the martensitic transition temperature of the sample with $x=0.35$, we carried out the DSC measurements. Figure 7 shows the DSC curves of the sample with $x=0.35$ for the heating and cooling processes. T_{Ms} , T_{Mf} , T_{As} and T_{Af} are determined by using the intersections of the baseline and the tangent lines with the largest slopes of the DSC peaks as shown in Fig. 7. Similar DSC curves were observed also for the sample with $x=0.40$.

Based on the above experimental results, the martensite-magnetization phase diagram of $Ni_2Mn_{1-x}Cu_xGa$ ($0 \leq x \leq 0.40$) was determined as shown in Fig. 8. In the compositional interval $0 \leq x \leq 0.23$, the Curie temperature decreases from $T_C \approx 374$ K at $x=0$ to $T_C=301.2$ K at $x=0.23$. The martensitic transition temperature T_M increases at first with increasing x . Further increase in x from $x=0.10$ to $x \approx 0.20$ does not affect T_M significantly, which remains almost constant around $T_M \approx 258$ K. As shown in Fig. 8, T_M and T_C merge together in samples with $0.23 \leq x \leq 0.30$. With further increase in x , T_M increases with increasing x from 331.3 K at $x=0.30$ to 478.5 K at $x=0.40$. To sum up, the following three

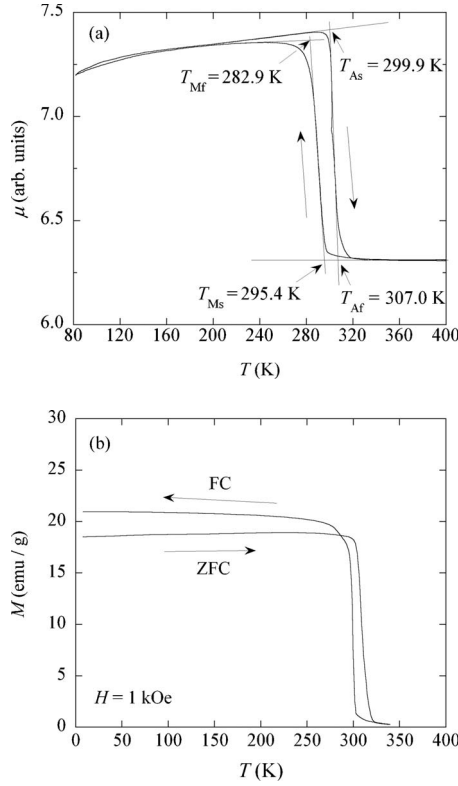


FIG. 5. Temperature dependences of (a) the initial permeability μ and (b) the magnetization M at 1 kOe for $\text{Ni}_2\text{Mn}_{0.77}\text{Cu}_{0.23}\text{Ga}$. The arrows along the curves in (a) show the cooling and heating processes. The arrows with ZFC and FC along the curves in (b) show the zero-field-cooling and field-cooling processes, respectively.

different concentration regions can be distinguished in the phase diagram shown in Fig. 8. The first region with $x \leq 0.23$ is characterized by $T_C > T_M$, i.e., the martensitic transition in the ferromagnetic state. The second region with $0.23 \leq x \leq 0.30$ is characterized by $T_M = T_C$, i.e., the coupled transitions of the martensite and ferromagnetic phases. In this compositional interval, the ferromagnetism also exhibits the first-order transition. Finally, the third region with $x > 0.30$ is characterized by $T_C < T_M$, i.e., the ferromagnetic transition in the martensitic state. It is remarkable that the phase diagram of $\text{Ni}_2\text{Mn}_{1-x}\text{Cu}_x\text{Ga}$ presented here has the characteristics very similar to those of the phase diagram of $\text{Ni}_{2+x}\text{Mn}_{1-x}\text{Ga}$ ($0 \leq x \leq 0.36$), which was already obtained by Khovaylo *et al.*²⁹ and Entel *et al.*³⁰ In the following, Secs. IV–VII, we try to understand the appearances of various phases in these alloys and the phase diagram by use of a phenomenological theory which improves the existing theories.^{27,29}

IV. PHENOMENOLOGICAL FREE ENERGY OF THE SYSTEM WITH THE MARTENSITIC AND FERROMAGNETIC PHASE TRANSITIONS

As shown in Sec. III, the various phases of $\text{Ni}_2\text{Mn}_{1-x}\text{Cu}_x\text{Ga}$, as well as those of $\text{Ni}_{2+x}\text{Mn}_{1-x}\text{Ga}$, are specified by the tetragonal distortion, the magnetization, and their coexistence. By assuming that both the distortion and

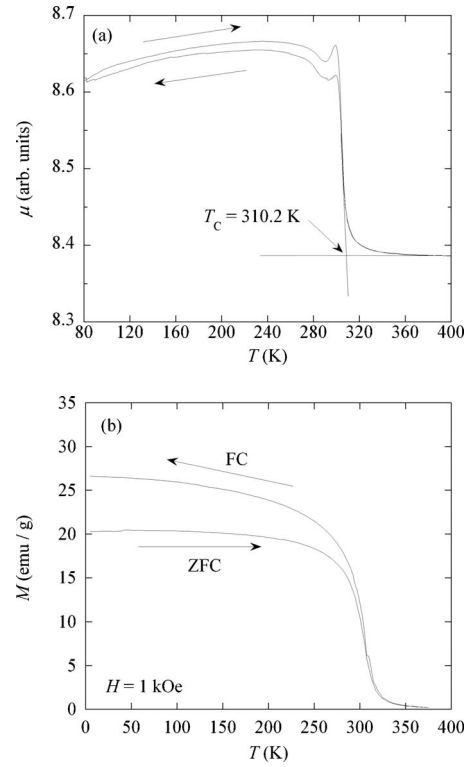


FIG. 6. Temperature dependences of (a) the initial permeability μ and (b) the magnetization M at 1 kOe for $\text{Ni}_2\text{Mn}_{0.65}\text{Cu}_{0.35}\text{Ga}$. The arrows along the curves in (a) show the cooling and heating processes. The arrows with ZFC and FC along the curves in (b) show the zero-field-cooling and field-cooling processes, respectively.

the magnetization are not subjected to spatial modulations, we take into account only the bulk crystal strains e_{ii} as possible order parameters of the martensitic phase transition and also the components of the magnetization M_i as possible order parameters of the ferromagnetic phase transition, i denoting the crystallographical axes, x , y , and z . In the following arguments, the off-diagonal strain components e_{ij} with $i \neq j$ are not contained for simplicity. The Landau free energy becomes a function of the strains e_{ii} and the magnetization components M_i , which should satisfy the cubic crystal symmetry of the Heusler $L2_1$ structure in the austenite phase and

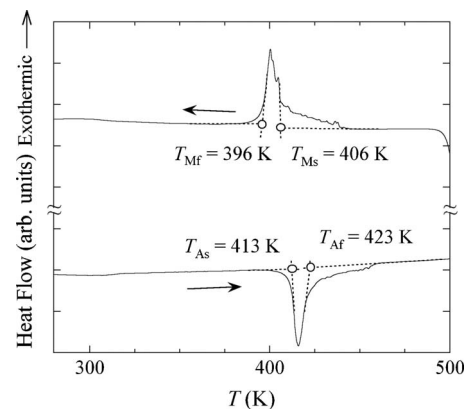


FIG. 7. DSC curves of $\text{Ni}_2\text{Mn}_{0.65}\text{Cu}_{0.35}\text{Ga}$. The arrows along the curves show the cooling and heating processes.

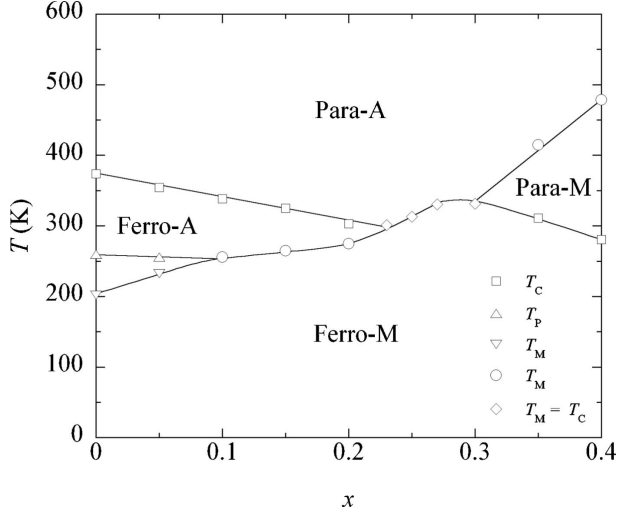


FIG. 8. Phase diagram of $\text{Ni}_2\text{Mn}_{1-x}\text{Cu}_x\text{Ga}$ ($0 \leq x \leq 0.4$). Para and Ferro mean paramagnetic and ferromagnetic states, respectively. A and M represent the austenite and martensite phases, respectively. T_p is the premartensitic transition temperature. T_C and T_M are the Curie temperature and the martensitic transition temperature, respectively. The data of the sample with $x=0$ were taken from Ref. 40. Solid lines in the figure are a guide for the eyes.

also the time-reversal symmetry. In order to describe the variety of the phases appearing in the alloys concerned with, the Landau free energy needs to be expanded in powers of the strains e_{ii} and the magnetization components M_i up to their fourth order. The resultant total free energy per unit volume consists of the three terms as follows:

$$F_{\text{tot}} = F_{\text{ela}} + F_{\text{mag}} + F_{\text{mag-ela}}. \quad (1)$$

The first term on the right-hand side of this equation, F_{ela} , is the free energy of the elastic strains e_{ii} . In finding the explicit form of this term, it is convenient to introduce the linear combinations of the strains e_{ii} , which are bases of the irreducible representations of the cubic group, as

$$e_1 = \frac{1}{\sqrt{3}}(e_{xx} + e_{yy} + e_{zz}), \quad (2)$$

$$e_2 = \frac{1}{\sqrt{2}}(e_{xx} - e_{yy}), \quad (3)$$

$$e_3 = \frac{1}{\sqrt{6}}(2e_{zz} - e_{xx} - e_{yy}). \quad (4)$$

A crystal-symmetry consideration gives

$$\begin{aligned} F_{\text{ela}} = & \frac{1}{2}\{c_1 e_1^2 + c_2(e_2^2 + e_3^2)\} + \frac{1}{3}\{A_1 e_1^3 + A_2 e_1(e_2^2 + e_3^2) \\ & + A_3 e_3(e_3^2 - 3e_2^2)\} + \frac{1}{4}\{I_1 e_1^4 + I_2 e_1^2(e_2^2 + e_3^2) \\ & + I_3 e_1 e_3(e_3^2 - 3e_2^2) + I_4(e_2^2 + e_3^2)^2\}, \end{aligned} \quad (5)$$

where the coefficients c_1 and c_2 , the coefficients A_1 , A_2 , and A_3 , and the coefficients from I_1 to I_4 can be expressed in

terms of the second-, third-, and fourth-order elastic moduli, respectively. The coefficients other than A_1 , A_2 , A_3 , and I_3 should be positive to stabilize the crystal. The second term in Eq. (1) is the free energy of the magnetic system, which is easily found to have the form as

$$F_{\text{mag}} = \frac{1}{2}\chi^{-1}\mathbf{M}^2 + \frac{1}{4}J_1\mathbf{M}^4 + K_1(M_y^2 M_z^2 + M_z^2 M_x^2 + M_x^2 M_y^2). \quad (6)$$

Here, χ^{-1} is the inverse of the magnetic susceptibility, J_1 originates mainly from the magnetic exchange energy, and K_1 is the magnetic anisotropy constant. The final term in Eq. (1), $F_{\text{mag-ela}}$, is the free energy of the coupling between the elastic strain and the magnetization. For the sake of the following arguments, this term is expanded in powers of e_{ii} up to its third order and of M_i up to its second order by neglecting other higher order couplings. The crystal symmetry and the time-reversal symmetry require that this term has the form as

$$\begin{aligned} F_{\text{mag-ela}} = & \left\{ B_1 e_1 + \frac{1}{2}[G_1 e_1^2 + G_2(e_2^2 + e_3^2)] \right. \\ & + \frac{1}{3}[P_1 e_1^3 + P_2 e_1(e_2^2 + e_3^2) + P_3 e_3(e_3^2 - 3e_2^2)] \left. \right\} \mathbf{M}^2 \\ & + \left\{ B_2 + \frac{1}{2}G_3 e_1 + \frac{1}{3}[P_4 e_1^2 + P_5(e_2^2 + e_3^2)] \right\} \\ & \times \left\{ e_2 \frac{1}{\sqrt{2}}(M_x^2 - M_y^2) + e_3 \frac{1}{\sqrt{6}}(2M_z^2 - M_x^2 - M_y^2) \right\} \\ & + \left\{ \frac{1}{2}G_4 + \frac{1}{3}P_6 e_1 \right\} \left\{ (e_3^2 - e_2^2) \frac{1}{\sqrt{6}}(2M_z^2 - M_x^2 - M_y^2) \right. \\ & \left. - 2e_2 e_3 \frac{1}{\sqrt{2}}(M_x^2 - M_y^2) \right\}. \end{aligned} \quad (7)$$

In the above equation, the coefficients B_1 and B_2 , the coefficients from G_1 to G_4 , and the coefficients from P_1 to P_6 are, respectively, the coupling constants between the linear, quadratic, and cubic terms of the elastic strains and the quadratic terms of the magnetizations. The terms with the coefficients B_1 and B_2 cause magnetostrictions in the ferromagnetic state, and also produce a uniaxial magnetic anisotropy energy in martensitic states. The terms with the coefficients from G_1 to G_4 , on the other hand, affect directly both the martensite and ferromagnetic phases by changing their transition temperatures. Among them, the terms with any of G_3 , G_4 , P_4 , P_5 , and P_6 also produce uniaxial magnetic anisotropy energies in martensitic states.

Although we confined ourselves to the case of spatially uniform order parameters in deriving the above free energies, there are still too many order parameters e_{ii} and M_i . In the present analyses, we do not exhaust all studies of many possible phases composed of these order parameters but take into account only order parameters to understand the ordered states (except for the premartensite phase) observed in $\text{Ni}_2\text{Mn}_{1-x}\text{Cu}_x\text{Ga}$. Because of this aim, we consider in the

following the case where only a tetragonal strain parallel to a crystallographical axis, say the z axis, can occur below the martensitic and/or ferromagnetic transition temperature, and a magnetization appears along a crystallographical axis, say the i axis, below the Curie temperature, i.e.,

$$e_3 \neq 0, \quad e_1 = e_2 = 0, \quad (8)$$

$$|\mathbf{M}| = M = M_i \neq 0. \quad (9)$$

Then, the free energy F_{tot} given by Eqs. (1)–(9) is reduced to

$$\begin{aligned} F_{\text{tot}} = & \frac{1}{2}c_2e_3^2 + \frac{1}{3}A_3e_3^3 + \frac{1}{4}I_4e_3^4 + \frac{1}{2}\chi^{-1}\mathbf{M}^2 + \frac{1}{4}J_1\mathbf{M}^4 \\ & + B_2e_3\kappa(\theta)\mathbf{M}^2 + \frac{1}{2}\{G_2 + G_4\kappa(\theta)\}e_3^2\mathbf{M}^2 \\ & + \frac{1}{3}\{P_3 + P_5\kappa(\theta)\}e_3^3\mathbf{M}^2, \end{aligned} \quad (10)$$

where

$$\kappa(\theta) = (3 \cos^2 \theta - 1)/\sqrt{6} \quad (11)$$

with $\theta=0$ for $\mathbf{M}\parallel\mathbf{c}$ and $\theta=\pi/2$ for $\mathbf{M}\perp\mathbf{c}$. From Eqs. (5) and (6), we see easily that the equilibrium ordered states given by Eqs. (8) and (9) can be realized under the following conditions:

$$I_4 > 0, \quad J_1 > 0, \quad \text{and} \quad K_1 > 0. \quad (12)$$

The signs of c_2 and χ^{-1} vary depending on temperature, dominating stabilities of phases.

Here we compare the above free energies given by Eqs. (1)–(12) with those which were considered by Vasil'ev *et al.*^{27,37} and Khovaylo *et al.*²⁹ in analyzing the phase diagram observed for $\text{Ni}_{2+x}\text{Mn}_{1-x}\text{Ga}$. Their free energies do not contain the magnetoelastic coupling terms with the coefficients from G_1 to G_4 in our free energy given by Eqs. (7) and (10), which play an essential role in the interplay of the martensite and ferromagnetic states in the present theory. In Khovailo *et al.*'s theory, the volume strain $e_1 = -A_2e_3^2/3c_1$, which is caused by an assumed martensitic distortion e_3 through a lattice anharmonic term in Eq. (5), plays an essential role in the interplay of the martensitic and ferromagnetic states. They showed that substitution of this volume strain e_1 into the term of $B_1e_1\mathbf{M}^2$ in Eq. (7) creates a term $-(A_2B_1/3c_1)e_3^2\mathbf{M}^2$. We notice, however, that this quantity is further written as $(A_2/3)(e_{1f}/e_3)e_3^3$, where $e_{1f} = -(B_1\mathbf{M}^2/c_1)$ is the volume magnetostriction with magnitudes of orders around 10^{-4} (Refs. 29 and 41) but e_3 is the martensitic distortion of orders $10^{-1} \sim 10^{-2}$. This suggests that the contribution of this volume-strain mechanism to the $e_3^2\mathbf{M}^2$ term is considerably small compared with lattice anharmonic terms. As will be shown in Sec. VII by numerical calculations, however, the effect of the lattice anharmonic energy should be comparable with that of the $e_3^2\mathbf{M}^2$ term for obtaining an agreement between the theory and the experiments. In Eq. (10), therefore, all effects of the volume strain e_1 were already neglected. On the other hand, the term with B_2 in Eq. (10) was the origin of the interplay of the two states in Vasil'ev *et al.*'s theory²⁷ but was neglected in Khovailo *et*

al.'s theory.²⁹ In the present theory, this term causes a magnetic anisotropy energy under martensitic distortions, rather than the interplay of the two states, as will be seen in the following sections. The final term with P_3 and P_5 in Eq. (10), which was not taken into account in the former theories, is necessary for an overall understanding of the observed phase diagrams.

V. FREE ENERGY FOR THE PHASE DIAGRAM IN THE TEMPERATURE-CONCENTRATION PLANE

In order to derive the phase diagram in the temperature T -concentration x plane observed on $\text{Ni}_2\text{Mn}_{1-x}\text{Cu}_x\text{Ga}$, we need to know the T and x dependences of the coefficients in the free energy given by Eq. (10). As in the usual Landau theory, it is assumed that the coefficients c_2 and χ^{-1} depend linearly on temperature T and vanish, respectively, at characteristic temperatures $T_M(x)$ and $T_C(x)$ at each concentration x , and that the other coefficients are all independent of T . Then, c_2 and χ^{-1} are expressed as

$$c_2 = \frac{c_m}{T_M(1)}[T - T_M(x)], \quad (13)$$

$$\chi^{-1} = \frac{c_f}{T_C(0)}[T - T_C(x)], \quad (14)$$

where c_m and c_f are defined to be positive constants independent of T and x . $T_M(x)$ is a latent second-order transition temperature of the martensitic distortion, and $T_C(x)$ is a latent or sometimes real second-order transition temperature of the ferromagnetic state, when the martensitic and ferromagnetic states appear spontaneously by themselves. Otherwise, $T_M(x)$ and/or $T_C(x)$ can be negative.

Also for the concentration x dependences of the coefficients in Eq. (10), we make the assumption that only c_2 and χ^{-1} depend on x through $T_M(x)$ and $T_C(x)$ but other coefficients are all independent of x . Here, the simplest x dependences of $T_M(x)$ and $T_C(x)$ are employed as follows:

$$T_M(x) = T_M(0) + [T_M(1) - T_M(0)]x, \quad (15)$$

$$T_C(x) = T_C(0) + [T_C(1) - T_C(0)]x. \quad (16)$$

The observed phase diagram shown in Fig. 8 directly shows that $T_M(x)$ at high concentrations and $T_C(x)$ at low concentrations are positive in $\text{Ni}_2\text{Mn}_{1-x}\text{Cu}_x\text{Ga}$.

To make easier the treatment of the free energy, we measure the various quantities in their suitable units as follows:

$$t = T/T_C(0), \quad (17)$$

$$t_m(x) = T_M(x)/T_C(0) = t_m(0) + [t_m(1) - t_m(0)]x, \quad (18)$$

$$t_c(x) = T_C(x)/T_C(0) = 1 + [t_c(1) - 1]x, \quad (19)$$

$$\bar{e}_3 = e_3/\sqrt{c_m/I_4}, \quad (20)$$

$$\bar{M} = M/\sqrt{c_f/J_1} \quad (21)$$

and

$$\bar{F}_{\text{tot}}(\bar{e}_3, \bar{M}) = F_{\text{tot}}(e_3, M)/(c_f^2/J_1). \quad (22)$$

After Eqs. (17)–(22) are substituted into Eq. (10), Eq. (10) has a simple form as

$$\begin{aligned} \bar{F}(\bar{e}_3, \bar{M}) = & \frac{1}{2}[t - t_c(x)]\bar{M}^2 + \frac{1}{4}\bar{M}^4 + r \left\{ \frac{1}{2t_m(1)}[t - t_m(x)]\bar{e}_3^2 \right. \\ & \left. + \frac{2}{3}a\bar{e}_3^3 + \frac{1}{4}\bar{e}_3^4 \right\} + \left(b + \frac{1}{2}g\bar{e}_3 + \frac{1}{3}p\bar{e}_3^2 \right) \bar{e}_3\bar{M}^2, \quad (23) \end{aligned}$$

where the new coefficients were defined as follows:

$$r = (c_m/c_f)^2(J_1/I_4), \quad (24)$$

$$a = (1/2\sqrt{c_m I_4})A_3, \quad (25)$$

$$b = (1/c_f)\sqrt{c_m/I_4}B_2\kappa(\theta), \quad (26)$$

$$g = (c_m/c_f I_4)\{G_2 + G_4\kappa(\theta)\} \quad (27)$$

and

$$p = (1/c_f)(c_m/I_4)^{3/2}\{P_3 + P_5\kappa(\theta)\}. \quad (28)$$

The values of b, g and p depend on the direction of the magnetization but are regarded as constants when any magnetic reorientation does not occur in the t - x plane. The criterion for this assumption is discussed in Appendix A, where the magnetic easy axis and the condition for occurrence of a magnetic reorientation are given.

VI. ORDER PARAMETERS IN THE VARIOUS PHASES

As seen in Fig. 8, $\text{Ni}_2\text{Mn}_{1-x}\text{Cu}_x\text{Ga}$, as well as $\text{Ni}_{2+x}\text{Mn}_{1-x}\text{Ga}$, exhibits the five different phases in the t - x plane, i.e., the paramagnetic and austenite phase labeled I, the paramagnetic and martensite phase labeled II, the ferromagnetic and austenite phase labeled III, the ferromagnetic and martensite phase labeled IV, and the premartensite phase labeled V. In this section, the order parameters in these phases are described.

A. Phase II

Equation (23) gives the free energy of the system in the phase II as

$$\bar{F}_{\text{II}}(\bar{e}_3, 0) = r \left\{ \frac{1}{2t_m(1)}[t - t_m(x)]\bar{e}_3^2 + \frac{2}{3}a\bar{e}_3^3 + \frac{1}{4}\bar{e}_3^4 \right\}. \quad (29)$$

By minimizing this free energy with respect to \bar{e}_3 , the equilibrium order parameter \bar{e}_3 in this phase is shown to be given by

$$\bar{e}_3 = -a - \text{sgn } a \sqrt{a^2 - \{[t - t_m(x)]/t_m(1)\}}. \quad (30)$$

It is noticed that \bar{e}_3 and a have opposite signs.

B. Phase III

In this phase, any pure martensitic distortion, i.e., the distortion which persists without the aid of the magnetization

\bar{M} , does not occur, but the magnetization can induce the magnetostriction. When the free energy given by Eq. (23) except for the terms of \bar{e}_3^3 and \bar{e}_3^4 is minimized with respect to \bar{e}_3 , the magnetostriction is found to be approximately given by

$$\bar{e}_3 = - \frac{b\bar{M}^2}{[r/t_m(1)][t - t_m(x)] + g\bar{M}^2}. \quad (31)$$

Then, the free energy of the phase III as a function of \bar{M} becomes

$$\bar{F}_{\text{III}}(\bar{e}_3, \bar{M}) = \frac{1}{2}[t - t_c(x)]\bar{M}^2 + \frac{1}{4} \left\{ 1 - \frac{2b^2 t_m(1)}{r[t - t_m(x)]} \right\} \bar{M}^4. \quad (32)$$

This free energy gives the equilibrium \bar{M} as

$$\bar{M} = \sqrt{\frac{[t_c(x) - t][t - t_m(x)]}{t - t_m(x) - (2/r)b^2 t_m(1)}} \quad (33)$$

at temperatures t sufficiently higher than $\{t_m(x) + (2/r)b^2 t_m(1)\}$.

C. Phase IV

The free energy given by Eq. (23) itself is minimized with respects to both \bar{e}_3 and \bar{M} . First, the equilibrium \bar{M} under a nonvanishing \bar{e}_3 is obtained to be

$$\bar{M} = \sqrt{t_c(x) - 2b - g\bar{e}_3^2 - (2/3)p\bar{e}_3^3 - t}. \quad (34)$$

When this equation is substituted into Eq. (23), the free energy of the system in the phase IV is expressed in terms of only \bar{e}_3 as

$$\begin{aligned} \bar{F}_{\text{IV}}(\bar{e}_3, \bar{M}) = & -\frac{1}{4} \left\{ [t - t_c(x)] + 2b\bar{e}_3 + g\bar{e}_3^2 + \frac{2}{3}p\bar{e}_3^3 \right\}^2 \\ & + r \left\{ \frac{1}{2t_m(1)}[t - t_m(x)] + \frac{2}{3}a\bar{e}_3 + \frac{1}{4}\bar{e}_3^2 \right\} \bar{e}_3^2. \quad (35) \end{aligned}$$

The equilibrium \bar{e}_3 is found by solving $\partial \bar{F}_{\text{IV}}(\bar{e}_3, \bar{M}) / \partial \bar{e}_3 = 0$. Because of the presence of the terms with b and p , however, its exact solution is too complicated, so that the equilibrium \bar{e}_3 is given only for $b=p=0$ as follows:

$$\begin{aligned} \bar{e}_3 = & -\frac{r}{r-g^2} \left(a + \text{sgn } a \right. \\ & \left. \times \sqrt{a^2 - \left(\frac{r-g^2}{r} \right) \left\{ \frac{1}{t_m(1)}[t - t_m(x)] - \frac{g}{r}[t - t_c(x)] \right\}} \right). \quad (36) \end{aligned}$$

As seen from this equation, \bar{e}_3 diverges as $r \rightarrow g^2$. This means that another term of \bar{e}_3^6 , which is not contained in the free energy in Eq. (23), is needed to stabilize the phase IV when r approaches to g^2 . This case is out of the scope of our analyses.

D. Phase V

As seen in Fig. 3(b), the magnetization is hardly affected by the transition from the phase III into the phase V although a tiny dip is observed in the temperature dependence of the magnetization. This implies that another order parameter occurs to coexist with the main order parameter of the uniform magnetization. In the premartensite phase of Ni_2MnGa , phonon softenings in the dispersion curve of the TA_2 mode have been already found by neutron scattering experiments.^{42,43} On the basis of this observation, Vasil'ev *et al.*³⁷ tried to analyze this phase by considering a long-period lattice structure. Since, however, the extra order parameter in this phase has not yet been settled, this phase is left to be open also in the present analyses.

As the result, our task becomes to find the temperature of the transition from the phase N into the phase N' (N, N' = I, II, III, and IV), $t_{c,N \leftrightarrow N'}(x)$. In Appendix B, some phase boundary lines are analytically derived in order to see their properties and to obtain guides to numerical calculations.

VII. NUMERICAL CALCULATIONS OF THE PHASE DIAGRAM

In this section, the phase diagram in the t - x plane is calculated numerically to compare the theory and the experiments on $\text{Ni}_2\text{Mn}_{1-x}\text{Cu}_x\text{Ga}$. In the numerical calculations, the values of some parameters are chosen so as to give an agreement between the theory and experiments. At first, Eqs. (B1) and (B2) are compared with the observed $t_{c,I \leftrightarrow II}(x)$ and $t_{c,I \leftrightarrow III}(x)$ in Fig. 8 to result in

$$t_c(1) = 0.11, \quad (37)$$

$$t_m(1) = \frac{3.46}{1 + (8/9)a^2}, \quad (38)$$

$$t_m(0) = -3.68 + t_m(1). \quad (39)$$

Under these conditions, we investigate the contribution of the b term to the phase diagram. This b term is known to be able to cause the magnetostructural transition without the g term.²⁷ The inset in Fig. 9 shows the phase diagram calculated for a chosen set of the values as $r=0.32$, $b=-0.08$, $a=-0.7$, and $g=p=0$. As seen from this figure, b has a large magnitude to give rise to the magnetostructural transition in a wide region of concentration. Moreover, the calculated phase boundary line between the phases III and IV is terminated at a critical concentration x_c and disappears below this x_c , being in disagreement with the observed phase diagram. Such the terminal point at x_c can appear for large magnitudes of b because the phases III and IV have the same crystallographical and magnetic symmetries for $b \neq 0$.³⁷ On the other hand, it is derived from Eq. (23) that \bar{e}_{3f}/\bar{e}_3 and $b\bar{M}^2/r$ can have similar orders, where \bar{e}_{3f} and \bar{e}_3 are a pure magnetostriction in a ferromagnetic state in the absence of the elastic softening by the martensitic transition and the martensitic distortion itself, respectively. If $\bar{e}_{3f} \sim 10^{-4}$ as in usual ferromagnets, and $\bar{e}_3 \sim 10^{-1}$ and $\bar{M}^2/r \sim 10^0$ as in the calculation

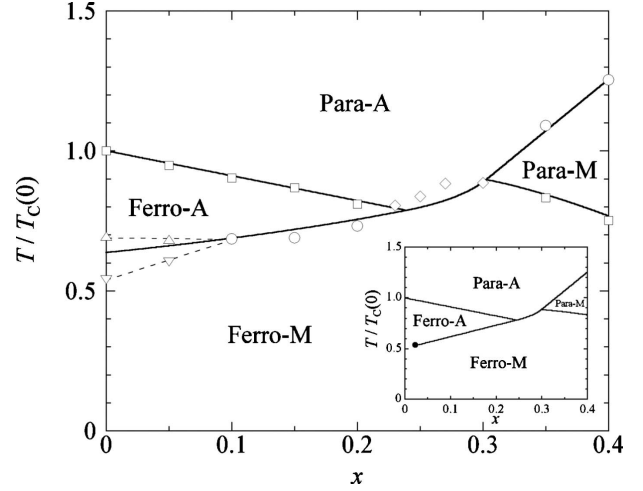


FIG. 9. Calculated phase diagram in the temperature t -concentration x plane of $\text{Ni}_2\text{Mn}_{1-x}\text{Cu}_x\text{Ga}$ with the experimental data. The solid lines are the calculated results obtained by use of the parameter values given in the text. The symbols are the experimental data taken from Fig. 8. A and M represent the austenite and martensite phases, respectively. The phase boundary line between the phases III (Ferro-A) and IV (Ferro-M) was obtained by neglecting the observed premartensite phase, whose boundaries are shown by the broken lines as a guide for the eyes. The inset shows the phase diagram calculated on the assumption that the magnetostriction is responsible for the magnetostructural transition. The black circle represents the terminal point of the phase boundary between the phases III (Ferro-A) and IV (Ferro-M). For the used values of the parameters, see the text.

given below are assumed, b is estimated to be of the order of 10^{-3} , which is much smaller than those of a, g and p in the following calculations. From these considerations, we assume that the b term can be neglected in determining the phase diagram of $\text{Ni}_2\text{Mn}_{1-x}\text{Cu}_x\text{Ga}$. As the result, the remaining parameters whose values can be chosen are r, a, g and p .

Before calculating the phase diagram of the real alloy system, some phase diagrams were calculated for model alloy systems in order to see the roles of the various terms in Eq. (23). Figure 10 shows the g dependence of the phase diagram, which was calculated for $r=0.324$ and $a=p=0$ under the fixed conditions Eqs. (37)–(39). As seen in this figure, the region of the phase IV is expanded or narrowed for a negative or a positive value of g , respectively. This is because the martensitic and ferromagnetic states are attractive or repulsive to each other, depending on the sign of g . All transitions are of the second order and any magnetostructural transition between the phases I and IV does not occur. When the a term becomes nonvanishing, the phase diagram is drastically changed as shown in Fig. 11. This figure shows the phase diagram calculated with $a=-0.7$ under the same values of the other parameters as those in Fig. 10. As seen from this figure, the transition temperatures $t_{c,I \leftrightarrow II}$ are considerably raised by the anharmonic a term, and the crossing point of the phase boundary lines between the phases I and II and between the phases I and III is shifted toward a low concentration. When $g < 0$, the magnetostructural transition occurs near the crossing point of the two phase boundary lines. In

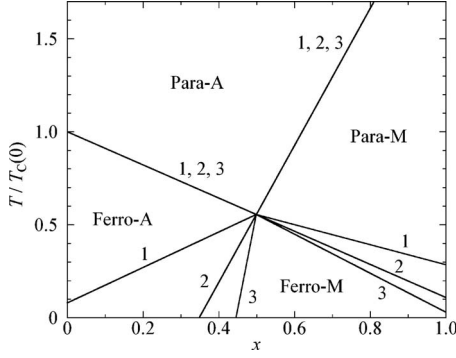


FIG. 10. Calculated phase diagrams in the temperature t -concentration x plane for model alloy systems. The phase diagrams were calculated for the three different values of g under $a=b=p=0$ and Eqs. (37)–(39). The lines 1, 2 and 3 are obtained for $g=-0.2, 0$, and 0.08 , respectively. A and M represent the austenite and martensite phases, respectively. For each value of g , the diagram is spanned by the four phases I(Para-A), II(Para-M), III(Ferro-A), and IV(Ferro-M).

the case of $g > 0$, on the other hand, the phase diagram becomes complicated near this crossing point and a reentrant ferromagnetism can occur with increasing t in a narrow concentration region around the concentration corresponding to the crossing point. Such the reentrant ferromagnetism has been already found in $\text{Ni}_2\text{Mn}_{1+x}\text{Sn}_{1-x}$,⁴⁴ $\text{Ni}_2\text{Mn}_{1-x}\text{In}_{1-x}$,⁴⁵ and $\text{Ni}_{50-x}\text{Co}_x\text{Mn}_{50-y}\text{In}_y$,⁴⁶ being studied in a more detail elsewhere. The phase transitions between the phases I and II, those between the phases I and IV, and those between the phases III and IV are of the first order because of the presence of the a term. (See Appendix B.) Therefore, the occurrence of the magnetostructural transition is considered to result from the cooperation of the attractive interaction between the martensite and ferromagnetic states and the first-order transition caused by the lattice anharmonicity. As seen from this figure, the transition temperatures $t_{c,\text{II}\leftrightarrow\text{IV}}$ in the martensite phase are drastically raised from the ferromag-

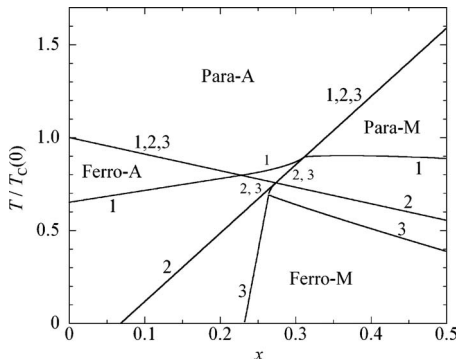


FIG. 11. Calculated phase diagrams in the temperature t -concentration x plane for model alloy systems. The phase diagrams were calculated for the three different values of g under $a=-0.7, b=p=0$, and Eqs. (37)–(39). The lines 1, 2 and 3 are obtained for $g=-0.2, 0$, and 0.08 , respectively. A and M represent the austenite and martensite phases, respectively. For each value of g , the diagram is spanned by the four phases I(Para-A), II(Para-M), III(Ferro-A), and IV(Ferro-M).

netic transition temperatures in the absence of the martensitic distortion by the attractive interaction between the two states, and $t_{c,\text{II}\leftrightarrow\text{IV}}$ becomes only weakly dependent on x . Moreover, the transition temperature $t_{c,\text{III}\leftrightarrow\text{IV}}$ depends linearly on x , as expected from Eq. (B7). These phase diagrams do not fully agree with the observed phase diagram of $\text{Ni}_2\text{Mn}_{1-x}\text{Cu}_x\text{Ga}$ shown in Fig. 8. This disagreement between the calculated and observed phase diagrams can be dissolved by taking into account the term with $p \neq 0$ in the free energy given by Eq. (23), as seen just below.

In the main panel of Fig. 9, we show the calculated phase diagram of $\text{Ni}_2\text{Mn}_{1-x}\text{Cu}_x\text{Ga}$ and compare this phase diagram with the observed one shown in Fig. 8. The chosen values of the parameters are as follows:

$$r = 0.324, \quad a = -0.706, \quad g = -0.547, \quad \text{and} \quad p = 0.572. \quad (40)$$

As seen in this figure, the agreement between the calculated and observed phase diagrams is satisfactory (except for the appearance of the premartensite phase). The term with g gives an attraction between the martensitic and ferromagnetic states, while the term with p gives a repulsion between the two states. The repulsion by the latter term becomes stronger with the larger martensitic distortions at higher concentrations x so that the martensitic state suppresses more strongly the appearance of the ferromagnetic state at higher concentrations x . This is the reason for that the calculated transition temperature $t_{c,\text{II}\leftrightarrow\text{IV}}$ decreases with increasing x as observed. Equations (18) and (38)–(40) give

$$t_m(x) = -1.28 + 3.68x. \quad (41)$$

This shows that $t_m(x)$ becomes negative for $x < 0.348$. Therefore, the observed martensitic states with high transition temperatures at low concentrations are stabilized by the attractive interaction between the martensitic and ferromagnetic states in addition to the lattice anharmonic energy.

In order to see explicitly the properties of each phase and its transition, we show in Fig. 12 the temperature dependences of the order parameters which were calculated by use of the same parameter values as those given by Eq. (40). As seen in this figure, the martensitic distortions \bar{e}_3 vanish always discontinuously at the martensitic transition temperatures $t_{c,\text{I}\leftrightarrow\text{II}}$, $t_{c,\text{III}\leftrightarrow\text{IV}}$, and $t_{c,\text{I}\leftrightarrow\text{IV}}$. The magnetizations \bar{M} , on the other hand, vanish continuously at $t_{c,\text{I}\leftrightarrow\text{III}}$ and $t_{c,\text{II}\leftrightarrow\text{IV}}$ so that the magnetic transitions at these temperatures are of the second order. However, the magnetizations \bar{M} also change discontinuously at $t_{c,\text{III}\leftrightarrow\text{IV}}$ and $t_{c,\text{I}\leftrightarrow\text{IV}}$. From Eqs. (17), (22), and (23), we see that the increase in the total entropy by a transition from the phase N to the phase N' with increasing temperature t is given by the sum of the entropy increase in the ferromagnetic system, ΔS_f , and that of the martensitic system, ΔS_m , as

$$\Delta S = \Delta S_f + \Delta S_m, \quad (42)$$

$$\Delta S_f = \frac{c_f^2}{2J_1 T_C(0)} \{(\bar{M}_N)^2 - (\bar{M}_{N'})^2\}, \quad (43)$$

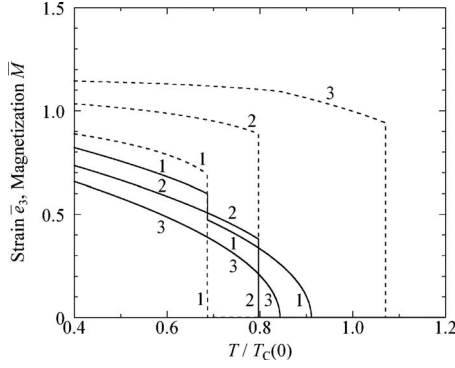


FIG. 12. Calculated temperature dependences of the order parameters at three different concentrations x . The solid lines are the calculated magnetizations \bar{M} while the broken lines are the calculated distortions \bar{e}_3 . The lines 1 were obtained for $x=0.1$ in the concentration region where the first order transition between the phases III and IV occurs. The lines 2 were obtained for $x=0.25$ in the concentration region where the magnetostructural transition occurs. The lines 3 were obtained for $x=0.35$ in the concentration region where the second-order transition occurs between the phases II and IV. The used values of the parameters are same as those for the phase diagram in the main panel of Fig. 9.

$$\Delta S_m = \frac{c_m^2}{2I_4 T_M(1)} \{(\bar{e}_{3,N})^2 - (\bar{e}_{3,N'})^2\}, \quad (44)$$

where \bar{M}_N and $\bar{e}_{3,N}$ are the order parameters in the phase N. Equations (43) and (44) prove that a discontinuous change of one of the two order parameters accompanies a discontinuous change in the entropy, and therefore the first-order transition, of the system with that order parameter. As the result, the transitions of the martensitic system at $t_{c,I \leftrightarrow II}$, $t_{c,III \leftrightarrow IV}$, and $t_{c,I \leftrightarrow IV}$, and also those of the ferromagnetic system at $t_{c,III \leftrightarrow IV}$ and $t_{c,I \leftrightarrow IV}$ are of the first order. Such the first-order transition of the ferromagnetic system is forced by the first-order transition of the martensitic system with the anharmonic energy through the attractive interaction between the two systems. The calculated continuous and discontinuous transitions of \bar{M} are consistent with the observations shown in Figs. 3(b), 4(b), 5(b), and 6(b). It is mentioned here that the phase boundary line between the phases III and IV in the main panel of Fig. 9 was calculated by neglecting the appearance of the premartensite phase V below $x < 0.1$.

Finally, it is noticed that the observed magnetization \bar{M} decreases below $t_{c,III \leftrightarrow IV}$ as shown in Fig. 4(b), contrary to the calculated result that \bar{M} increases below this transition temperature as seen in Fig. 12. This disagreement can be explained as follows. In a martensitic state with a large distortion, the uniaxial magnetic anisotropy energy given by Eq. (A10) becomes so large that the magnetization directs to the direction of the tetragonal distortion. When martensitic variants are distributed in the phase IV, magnetic domains with different directions are inevitably distributed. Nevertheless, magnetizations are not saturated to equilibrium magnetizations in measuring magnetizations under a small magnetic field, $H=1$ kOe. In fact, the magnetization of the end mem-

ber of this alloy system, Ni_2MnGa , which was determined by applying magnetic fields up to 10 T, increases with the transition from the phase V to the phase IV.^{47,48}

VIII. CONCLUDING REMARKS

Magnetization and initial permeability measurements were carried out on the ferromagnetic shape memory alloys $Ni_2Mn_{1-x}Cu_xGa$ ($0 \leq x \leq 0.4$). On the basis of the experimental results, the magnetic phase diagram of $Ni_2Mn_{1-x}Cu_xGa$ ($0 \leq x \leq 0.4$) was determined. The obtained phase diagram reveals that its characteristics, such as an inversion between T_C and T_M with increasing x and the appearance of the magnetostructural transition, are very similar to those in the phase diagram of $Ni_{2+x}Mn_{1-x}Ga$, except for the different concentration regions for the appearances of the magnetostructural transitions in the two alloy systems. The observed fact that the phase diagram is robust in spite of different constituent atoms in alloys may be suggestive in identifying the origin of the martensitic transition. Since both the substitutions of Cu and Ni for Mn in these alloys increase the values of the average number of valence electron per atom e/a , the similarity of the two phase diagrams does not contradict with an assumption that the martensitic transition has its origin in band electrons, as in the mechanism of the band Jahn-Teller effect.⁴⁹⁻⁵¹ However, the concentrations for the appearances of the magnetostructural transitions in $Ni_2Mn_{1-x}Cu_xGa$ are higher than those in $Ni_{2+x}Mn_{1-x}Ga$ in spite of the fact that Cu supplies valence electrons more than that of Ni. This result may imply that a simple picture on the basis of the rigid-band theory no longer holds.

In order to understand the phase diagram observed for $Ni_2Mn_{1-x}Cu_xGa$, we restudied the phenomenological theories on $Ni_{2+x}Mn_{1-x}Ga$ by Vasil'ev *et al.*^{27,37} and by Khovaylo *et al.*²⁹ and found that these theories should be improved by taking into account the energy of the higher order couplings between the strain and the magnetization. This improvement resolved the disagreements between the theories and the experimental results that Vasil'ev *et al.*'s theory^{27,37} gives a terminal point on the phase boundary line between the phases III and IV, and the phase transitions between the two phases vanish at low concentrations and that Khovaylo *et al.*'s theory²⁹ seems to need an extraordinary large magneto-volume strain. As the result, we could obtain the satisfactory agreement between the calculated and observed phase diagrams for $Ni_2Mn_{1-x}Cu_xGa$. The present theory confirms the followings: The magnetostructural transition can appear when the biquadratic coupling between the strain and the magnetization favors the coexistence of the strain and the magnetization and the martensitic transition is of the first order because of the presence of the lattice anharmonicity. The phase IV at low concentrations is realized by both the magnetoelastic coupling and the lattice anharmonicity although the martensitic distortion cannot appear spontaneously by itself. Since the magnetization and the martensitic distortion couples strongly to each other, the magnetizations are forced to change discontinuously on the phase boundary lines between the phases III and IV, and between the phases I and IV by the discontinuous changes in the martensitic

distortions on these lines. Further, it can be expected that one of an external stress and a magnetic field can affect considerably both the martensitic distortion and the magnetization through this strong coupling. This phenomenon becomes most conspicuous for alloys in which both the martensitic and ferromagnetic systems exhibit the first order transitions as the result of their strong coupling.

In conclusion, the phase diagram in the temperature-concentration plane was obtained experimentally for the Heusler-type alloy $\text{Ni}_2\text{Mn}_{1-x}\text{Cu}_x\text{Ga}$. It was found that this compound system also exhibits both the martensite phase, the ferromagnetic phase, and the coexisting phase of the martensitic and ferromagnetic states and that the overall feature of this phase diagram is very similar to that of $\text{Ni}_{2+x}\text{Mn}_{1-x}\text{Ga}$. The observed phase diagram was explained, except for the appearance of the premartensite phase, on the basis of the phenomenological theory, which improved the existing theories by taking account of the higher order couplings between the strain and the magnetization.

ACKNOWLEDGMENTS

This work was supported by a Grant-in-Aid for Scientific Research (C) (Grant No. 21560693) from the Japan Society for the Promotion of Science (JSPS). Part of this work was supported also by a Grant-in-Aid for Scientific Research (S) (Grant No. 22226021) from the Japan Society for the Promotion of Science (JSPS) and by the Global COE Program, Tohoku University, MEXT, Japan.

APPENDIX A: MAGNETIC EASY AXIS AND CONDITION FOR OCCURRENCE OF MAGNETIC REORIENTATION

Let us consider a state in which the lattice is subjected to the tetragonal distortion along the c axis and the magnetization is in the (010) plane. Then, we have

$$\bar{M}_z = \bar{M} \cos \theta, \quad \bar{M}_x = \bar{M} \sin \theta, \quad \text{and} \quad \bar{M}_y = 0, \quad (\text{A1})$$

where θ is the angle between the c axis and the magnetization. By use of Eqs. (6) and (23), the energy giving rise to the magnetic anisotropy, $\bar{F}_A(\theta)$, is shown to be expressed by

$$\bar{F}_A(\theta) = k_1 \bar{M}_z^2 \bar{M}_x^2 + \left(b \bar{e}_3 + \frac{1}{2} g \bar{e}_3^2 + \frac{1}{3} p \bar{e}_3^3 \right) \bar{M}^2 \quad (\text{A2})$$

with

$$k_1 = K_1/J_1. \quad (\text{A3})$$

Here, b , g , and p , which are given by Eqs. (26)–(28), depend on θ as

$$b = b_2 \kappa(\theta), \quad (\text{A4})$$

$$g = g_2 + g_4 \kappa(\theta) \quad (\text{A5})$$

and

$$p = p_3 + p_5 \kappa(\theta), \quad (\text{A6})$$

where

$$b_2 = (1/c_f) \sqrt{c_m/I_4} B_2, \quad (\text{A7})$$

$$g_\nu = (c_m/c_f I_4) G_\nu, \quad (\nu = 2, 4) \quad (\text{A8})$$

and

$$p_\nu = (1/c_f)(c_m/I_4)^{3/2} P_\nu, \quad (\nu = 3, 5). \quad (\text{A9})$$

Substitution of Eqs. (A4)–(A6) and (11) into Eq. (A2) gives

$$\begin{aligned} \bar{F}_A(\theta) = & \frac{3}{\sqrt{6}} \left(b_2 \bar{e}_3 + \frac{1}{2} g_4 \bar{e}_3^2 + \frac{1}{3} p_5 \bar{e}_3^3 \right) \bar{M}^2 \cos^2 \theta \\ & + (1/4) k_1 \bar{M}^4 \sin^2(2\theta), \end{aligned} \quad (\text{A10})$$

where terms independent of θ were neglected.

From Eq. (A10), we see that the magnetic easy axis is the c axis under $k_1 > 0$, when the condition

$$\left(b_2 + \frac{1}{2} g_4 \bar{e}_3 + \frac{1}{3} p_5 \bar{e}_3^2 \right) \bar{e}_3 < 0 \quad (\text{A11})$$

is satisfied. This is just the case where we have studied in the text. If a change in \bar{e}_3 , which depends on temperature t and concentration x , violates the condition (A11), a reorientation of the magnetization from the c axis to the a axis occurs at \bar{e}_3 satisfying

$$b_2 + \frac{1}{2} g_4 \bar{e}_3 + \frac{1}{3} p_5 \bar{e}_3^2 = 0. \quad (\text{A12})$$

Such a magnetic reorientation has not been investigated experimentally on $\text{Ni}_2\text{Mn}_{1-x}\text{Cu}_x\text{Ga}$.

APPENDIX B: ANALYSES OF THE PHASE BOUNDARY LINES

The phase boundary lines are briefly analyzed on the basis of Eq. (23). The analyses are done along a parallel way to those in Refs. 27 and 29.

1. Phase boundary line between the phases I and II

Since the transition between the phases I and II is of the first order, \bar{e}_3 and $t_{c,I \leftrightarrow II}(x)$ should satisfy $\bar{F}_{II}(\bar{e}_3, 0) = 0$ and $\partial \bar{F}_{II}(\bar{e}_3, 0) / \partial \bar{e}_3 = 0$, where $\bar{F}_N(\bar{e}_3, \bar{M})$ is the free energy in the phase N. These equations give

$$t_{c,I \leftrightarrow II}(x) = t_m(x) + (8/9) a^2 t_m(1). \quad (\text{B1})$$

2. Phase boundary line between the phases I and III

When $|b|$ is sufficiently small and the ferromagnetic transition is of the second order, the transition temperature in this case becomes $t_c(x)$ itself so that

$$t_{c,I \leftrightarrow III}(x) = 1 + (t_c(1) - 1)x. \quad (\text{B2})$$

3. Phase boundary line between the phases II and IV

When $|b|$ is again sufficiently small, the ferromagnetic transition is of the second order in the martensite phase. This gives

$$t_{c,II\leftrightarrow IV}(x) = t_c(x) - 2b\bar{e}_3 - g\bar{e}_3^2 - (2/3)p\bar{e}_3^3, \quad (\text{B3})$$

where \bar{e}_3 , which is given by Eq. (30), also depends on $t_{c,II\leftrightarrow IV}(x)$. This equation for $t_{c,II\leftrightarrow IV}(x)$ can be solved analytically for $b=p=0$ as follows:

$$\begin{aligned} t_{c,II\leftrightarrow IV}(x) &= t_m(x) - \{t_m(1)/[g - t_m(1)]^2\} \\ &\times \{[t_c(x) - t_m(x) - 2ga^2][g_2 - t_m(1)] + 2g^2a^2 \\ &- 2ga\sqrt{a^2t_m(1)^2 + [t_c(x) - t_m(x)][g - t_m(1)]}\}. \end{aligned} \quad (\text{B4})$$

4. Phase boundary line between the phases III and IV

The transition of \bar{e}_3 is discontinuous for $a \neq 0$ even in the presence of the magnetization. On this phase boundary, therefore, the following equations should be satisfied.

$$\frac{\partial}{\partial \bar{e}_3} \bar{F}_{IV}(\bar{e}_3, \bar{M}_{IV}) = 0, \quad \text{and} \quad \frac{\partial}{\partial \bar{M}_{IV}} \bar{F}_{IV}(\bar{e}_3, \bar{M}_{IV}) = 0, \quad (\text{B5})$$

$$\bar{F}_{III}(0, \bar{M}_{III}) = \bar{F}_{IV}(\bar{e}_3, \bar{M}_{IV}), \quad (\text{B6})$$

where \bar{M}_{III} is given by Eq. (33). Elimination of \bar{e}_3 and \bar{M}_{IV} from Eqs. (B5) and (B6) can be done only for $b=p=0$, which gives $t_{c,III\leftrightarrow IV}(x)$ as

$$\begin{aligned} t_{c,III\leftrightarrow IV}(x) &= \{1/[r - gt_m(1)]\} \\ &\times \left([rt_m(0) - gt_m(1)] + \frac{8}{9} \left(\frac{r^2}{r - g^2} \right) a^2 t_m(1) \right. \\ &\left. + \{r[t_m(1) - t_m(0)] - gt_m(1)[t_c(1) - 1]\}x \right). \end{aligned} \quad (\text{B7})$$

5. Phase boundary line between the phases I and IV

Also on this phase boundary line, the equilibrium \bar{e}_3 and \bar{M}_{IV} should satisfy Eq. (B5) but

$$\bar{F}_{IV}(\bar{e}_3, \bar{M}_{IV}) = 0. \quad (\text{B8})$$

Elimination of \bar{e}_3 and \bar{M}_{IV} from Eqs. (B5) and (B8) can be done analytically only for $b=p=0$ and $t_c(x) \approx t_m(x)$. Then, $t_{c,I\leftrightarrow IV}(x)$ is found to be expressed by Eq. (B7) with $t_{c,I\leftrightarrow IV}(x)$ replacing $t_{c,III\leftrightarrow IV}(x)$ and $a^2\Gamma$ replacing a^2 , where Γ is defined by

$$\begin{aligned} \Gamma &= \{1/2(1 - \gamma)^2\} \{(1 - 9\gamma) \\ &+ \text{sgn}(1 - \gamma) \sqrt{1 + 9\gamma + 27(1 + \gamma)\gamma^2}\} \end{aligned} \quad (\text{B9})$$

with

$$\gamma = t_m(1)^2(r - g^2)/\{r - gt_m(1)\}^2. \quad (\text{B10})$$

-
- ¹K. Ullakko, J. K. Huang, C. Kantner, R. C. O'Handley, and V. V. Kokorin, *Appl. Phys. Lett.* **69**, 1966 (1996).
- ²Y. Ma, A. Awaji, K. Watanabe, M. Matsumoto, and N. Kobayashi, *Solid State Commun.* **113**, 671 (2000).
- ³K. Oikawa, W. Ito, Y. Imano, Y. Sutou, R. Kainuma, K. Ishida, S. Okamoto, O. Kitakami, and T. Kanomata, *Appl. Phys. Lett.* **88**, 122507 (2006).
- ⁴T. Krenke, M. Acet, E. F. Wassermann, X. Moya, L. Mañosa, and A. Planes, *Phys. Rev. B* **73**, 174413 (2006).
- ⁵V. K. Sharma, M. K. Chattopadhyay, and S. B. Roy, *J. Phys.: Condens. Matter* **20**, 425210 (2008).
- ⁶W. Ito, K. Ito, R. Y. Umetsu, R. Kainuma, K. Koyama, K. Watanabe, A. Fujita, K. Oikawa, K. Ishida, and T. Kanomata, *Appl. Phys. Lett.* **92**, 021908 (2008).
- ⁷R. Y. Umetsu, Y. Kusakari, T. Kanomata, K. Suga, Y. Sawai, K. Kindo, K. Oikawa, R. Kainuma, and K. Ishida, *J. Phys. D: Appl. Phys.* **42**, 075003 (2009).
- ⁸R. Y. Umetsu, W. Ito, K. Ito, K. Koyama, A. Fujita, K. Oikawa, T. Kanomata, R. Kainuma, and K. Ishida, *Scr. Mater.* **60**, 25 (2009).
- ⁹T. Krenke, E. Duman, M. Acet, E. W. Wassermann, X. Moya, L. Mañosa, and A. Planes, *Nature Mater.* **4**, 450 (2005).
- ¹⁰T. Krenke, M. Acet, E. F. Wassermann, X. Moya, L. Mañosa, and A. Planes, *Phys. Rev. B* **72**, 014412 (2005).
- ¹¹R. Kainuma, Y. Imano, W. Ito, H. Morito, Y. Sutou, K. Oikawa, A. Fujita, K. Ishida, S. Okamoto, O. Kitakami, and T. Kanomata, *Appl. Phys. Lett.* **88**, 192513 (2006).
- ¹²D. L. Schlagel, W. M. Yuhasz, K. W. Dennis, R. W. McCallum, and T. A. Lograsso, *Scr. Mater.* **59**, 1083 (2008).
- ¹³T. Omori, K. Watanabe, R. Y. Umetsu, R. Kainuma, and K. Ishida, *Appl. Phys. Lett.* **95**, 082508 (2009).
- ¹⁴R. Kainuma, Y. Imano, W. Ito, Y. Sutou, H. Morito, S. Okamoto, O. Kitakami, K. Oikawa, A. Fujita, T. Kanomata, and K. Ishida, *Nature (London)* **439**, 957 (2006).
- ¹⁵Y. D. Wang, Y. Ren, E. W. Huang, Z. H. Nie, G. Wang, Y. D. Liu, J. N. Deng, L. Zuo, H. Choo, P. K. Liaw, and D. E. Brown, *Appl. Phys. Lett.* **90**, 101917 (2007).
- ¹⁶Y. D. Wang, E. W. Huang, Y. Ren, Z. H. Nie, G. Wang, Y. D. Liu, J. N. Deng, H. Choo, P. K. Liaw, D. E. Brown, and L. Zuo, *Acta Mater.* **56**, 913 (2008).
- ¹⁷R. Kainuma, K. Oikawa, W. Ito, Y. Sutou, T. Kanomata, and K. Ishida, *J. Mater. Chem.* **18**, 1837 (2008).
- ¹⁸H. E. Karaca, I. Karaman, B. Basaran, Y. Ren, Y. I. Chumlyakov, and H. J. Maier, *Adv. Funct. Mater.* **19**, 983 (2009).
- ¹⁹F. Hu, J. Sun, G. Wu, and B. Shen, *J. Appl. Phys.* **90**, 5216 (2001).
- ²⁰F. X. Hu, B. G. Shen, J. R. Sun, and G. H. Wu, *Phys. Rev. B* **64**, 132412 (2001).
- ²¹L. Paretì, M. Solzi, F. Albertini, and A. Paoluzi, *Eur. Phys. J. B* **32**, 303 (2003).
- ²²J. Marcos, L. Mañosa, A. Planes, F. Casanova, X. Batlle, A. Labarta, and B. Matínez, *J. Phys. IV* **115**, 105 (2004).
- ²³A. Aliev, A. Batdalov, S. Bosko, V. Buchelnikov, I. Dikshtein, V. Khovailo, V. Koledov, R. Levitin, V. Shavrov, and T. Takagi, *J.*

- Magn. Magn. Mater.* **272-276**, 2040 (2004).
- ²⁴A. Planes, L. Mañosa, X. Moya, J. Marcos, M. Acet, T. Krenke, S. Aksoy, and E. F. Wassermann, *Adv. Mater. Res.* **52**, 221 (2008).
- ²⁵A. Planes, L. Mañosa, and M. Acet, *J. Phys.: Condens. Matter* **21**, 233201 (2009).
- ²⁶M. Matsumoto, T. Takagi, J. Tani, T. Kanomata, N. Muramatsu, and A. N. Vasil'ev, *Mater. Sci. Eng., A* **273-275**, 326 (1999).
- ²⁷A. N. Vasil'ev, A. D. Bozhko, V. V. Khovailo, I. E. Dikshstein, V. G. Shavrov, V. D. Buchelnikov, M. Matsumoto, S. Suzuki, T. Takagi, and J. Tani, *Phys. Rev. B* **59**, 1113 (1999).
- ²⁸W. H. Wang, J. L. Chen, S. X. Gao, G. H. Wu, Z. Wang, Y. F. Zheng, L. C. Zhao, and W. S. Zhan, *J. Phys.: Condens. Matter* **13**, 2607 (2001).
- ²⁹V. V. Khovaylo, V. D. Buchelnikov, R. Kainuma, V. V. Koledov, M. Ohtsuka, V. G. Shavrov, T. Takagi, S. V. Taskaev, and A. N. Vasiliev, *Phys. Rev. B* **72**, 224408 (2005).
- ³⁰P. Entel, V. D. Buchelnikov, V. V. Khovailo, A. T. Zayak, W. A. Adeagbo, M. E. Gruner, H. C. Herper, and E. F. Wassermann, *J. Phys. D: Appl. Phys.* **39**, 865 (2006).
- ³¹M. Khan, I. Dubenko, S. Stadler, and N. Ali, *J. Appl. Phys.* **97**, 10M304 (2005).
- ³²A. M. Gomes, M. Khan, S. Stadler, N. Ali, I. Dubenko, A. Y. Takeuchi, and A. P. Guimarães, *J. Appl. Phys.* **99**, 08Q106 (2006).
- ³³S. Stadler, M. Khan, J. Mitchell, N. Ali, A. M. Gomes, I. Dubenko, A. Y. Takeuchi, and A. P. Guimarães, *Appl. Phys. Lett.* **88**, 192511 (2006).
- ³⁴C. Jiang, J. Wang, P. Li, A. Jia, and H. Xu, *Appl. Phys. Lett.* **95**, 012501 (2009).
- ³⁵B. R. Gautam, I. Dubenko, J. C. Mabon, S. Stadler, and N. Ali, *J. Alloys Compd.* **472**, 35 (2009).
- ³⁶A. T. Zayak, V. D. Buchelnikov, and P. Entel, *Phase Transitions* **75**, 243 (2002).
- ³⁷A. N. Vasil'ev, V. D. Buchel'nikov, T. Takagi, V. V. Khovailo, and É. I. Éstrin, *Phys. Usp.* **46**, 559 (2003).
- ³⁸T. Kanomata, T. Nozawa, D. Kikuchi, H. Nishihara, K. Koyama, and K. Watanabe, *Int. J. Appl. Electromagn. Mech.* **21**, 151 (2005).
- ³⁹T. Ohba, N. Miyamoto, K. Fukuda, T. Fukuda, T. Kakeshita, and K. Kato, *Smart Mater. Struct.* **14**, S197 (2005).
- ⁴⁰P. J. Brown, J. Crangle, T. Kanomata, M. Matsumoto, K.-U. Neumann, B. Ouladdiaf, and K. R. A. Ziebeck, *J. Phys.: Condens. Matter* **14**, 10159 (2002).
- ⁴¹J. Kanamori, in *Magnetism*, edited by G. T. Rado and H. Suhl (Academic Press, New York, 1963), Vol. 1, p. 127.
- ⁴²A. Zheludev, S. M. Shapiro, P. Wochner, A. Schwartz, M. Wall, and L. E. Tanner, *Phys. Rev. B* **51**, 11310 (1995).
- ⁴³X. Moya, D. González-Alonso, L. Mañosa, A. Planes, V. O. Garlea, T. A. Lograsso, D. L. Schlagel, J. L. Zarestky, S. Aksoy, and M. Acet, *Phys. Rev. B* **79**, 214118 (2009).
- ⁴⁴T. Kanomata, K. Fukushima, H. Nishihara, R. Kainuma, W. Ito, K. Oikawa, K. Ishida, K.-U. Neumann, and K. R. A. Ziebeck, *Mater. Sci. Forum* **583**, 119 (2008).
- ⁴⁵T. Kanomata, T. Yasuda, S. Sasaki, H. Nishihara, R. Kainuma, W. Ito, K. Oikawa, K. Ishida, K.-U. Neumann, and K. R. A. Ziebeck, *J. Magn. Magn. Mater.* **321**, 773 (2009).
- ⁴⁶W. Ito, Y. Imano, R. Kainuma, Y. Sutou, K. Oikawa, and K. Ishida, *Metall. Mater. Trans. A* **38**, 759 (2007).
- ⁴⁷V. V. Khovailo, V. Novosad, T. Takagi, D. A. Filippov, R. Z. Levitin, and A. N. Vasil'ev, *Phys. Rev. B* **70**, 174413 (2004).
- ⁴⁸P. J. Webster, K. R. A. Ziebeck, S. L. Town, and M. S. Peak, *Philos. Mag. B* **49**, 295 (1984).
- ⁴⁹M. Kataoka, *Phys. Lett.* **80A**, 35 (1980); *Phys. Rev. B* **28**, 2800 (1983).
- ⁵⁰M. Kataoka and N. Toyota, *Phase Transitions* **8**, 157 (1987).
- ⁵¹W. Weber and L. F. Mattheiss, *Phys. Rev. B* **25**, 2270 (1982).